MDPI

Evaluation of Thermal Stability and Its Effect on the Corrosion Behaviour of Mg-RE Alloys Processed by High-Pressure Torsion

Hiba Azzeddine [1,*], Abdelkader Hanna [1], Achour Dakhouche [2], Thierry Baudin [3], François Brisset [3], Yi Huang [4,5] and Terence G. Langdon [4]

[1] Laboratory of Materials and Renewable Energy, Faculty of Sciences, Mohamed Boudiaf University, M'sila 28000, Algeria
[2] Inorganic Materials Laboratory, Department of Chemistry, Faculty of Sciences, University of Mohamed Boudiaf, M'sila 28000, Algeria
[3] Université Paris-Saclay, CNRS, Institut de Chimie Moléculaire et des Matériaux d'Orsay, 91405 Orsay, France
[4] Materials Research Group, Department of Mechanical Engineering, University of Southampton, Southampton SO17 1BJ, UK
[5] Department of Design and Engineering, Faculty of Science and Technology, Bournemouth University, Poole, Dorset BH12 5BB, UK
[*] Correspondence: hiba.azzeddine@univ-msila.dz

Abstract: The evolutions of microstructure and texture and the corrosion behaviour of low light rare-earth containing Mg-1.4Nd and low heavy rare-earth containing Mg-0.6Gd and Mg-0.4Dy (wt.%) were evaluated and compared after processing by high-pressure torsion (HPT) and isochronal annealing at 250 and 450 °C for 1 h using electron backscatter diffraction (EBSD) and electrochemical tests in a 3.5% (wt.%) NaCl solution. The EBSD results show that dynamic recrystallisation (DRX) was restricted in the Mg-1.4Nd alloy which led to a heterogenous deformation microstructure whereas the Mg-0.6Gd and Mg-0.4Dy alloys exhibited a homogenous deformation microstructure formed mostly of equiaxed dynamically recrystallised DRX grains. The HPT processing caused the development of a deviated basal texture in the three alloys. A good thermal stability of the three alloys was noticed after annealing at 250 °C. By contrast, annealing at 450 °C led to a homogenous equiaxed microstructure and weakening of texture for the Mg-1.4Nd alloy and a heterogenous bimodal microstructure with a stable basal texture for the Mg-0.6Gd and Mg-0.4Dy alloys. The HPT-processed Mg–RE alloys exhibited an improved corrosion resistance due to grain refinement. Thereafter, the corrosion resistance of the Mg-0.6Gd and Mg-0.4Dy alloys decreased with increasing annealing temperature due to an increase in grain size while the corrosion resistance of the Mg-1.4Nd alloy was improved after annealing at 450 °C due to precipitation and texture weakening.

Keywords: high-pressure torsion; magnesium; rare-earth alloys; texture; thermal stability

1. Introduction

Adding alloying elements for microstructural modifications and employing deformation processing to achieve crystallographic texture weakening are the best procedures for designing new magnesium (Mg) alloys having excellent mechanical and corrosion properties [1,2]. Adding rare-earth (RE) alloying elements significantly increases the formability and decreases the anisotropy of pure Mg by changing the deformation mode and acting as an obstacle for dislocation and grain boundary motion [3–5]. It is believed that the occurrence of RE solute drag and the presence of second phases hinder the motion of dislocations and reduce the grain boundary mobility which cause an overall reduction in dynamic recrystallisation (DRX) and consequently change the microstructure and texture through annealing treatments [6–10]. Furthermore, adding RE elements can improve the corrosion performance of Mg-based alloys by decreasing the corrosion rate and promoting the formation of passive corrosion product films [11–15]. Consequently, Mg–RE alloys are

now widely used in automotive and aerospace industries [16]. For example, WE43 and E21 alloys are used to fabricate cross-car beams and seat frames [17]. Moreover, Mg–RE based alloys are promising candidates for biomaterial applications as temporary implant [18,19].

Based on their electron configuration, the RE elements are divided into two categories. Light RE elements (LREE) category comprising lanthanum (La), cerium (Ce), praseodymium (Pr), neodymium (Nd), samarium (Sm), and europium (Eu) and heavy RE elements (HREE) category containing gadolinium (Gd), terbium (Tb), dysprosium (Dy), holmium (Ho), erbium (Er), thulium (Tm), ytterbium (Yb), lutetium (Lu), scandium (Sc), and yttrium (Y) [15]. However, the role of each RE element and each category in controlling the inherent properties of Mg-based alloys is not yet illustrated. The major disadvantage of RE elements is their high cost, especially for HREE which restricted their engineering applications and limited their use only in the scientific research and academic areas. Today, several investigations can be found focusing on developing new Mg–RE alloys with low RE content having simultaneously excellent mechanical properties [6,20–25].

Among the existing severe plastic deformation (SPD) techniques, processing by high-pressure torsion (HPT) [26] is capable of deforming Mg-based alloys at room temperature (RT) without any cracking or segmentation due to the application of a high hydrostatic pressure [27]. This HPT processing produces bulk ultrafine-grained materials with a high fraction of high-angle boundaries leading to excellent mechanical and superplastic properties [28–35]. The grain refinement in Mg-based alloys usually occurs by DRX and the resultant grain size can reach a nano-size or micro-size scale depending on many parameters such as the alloy composition, the presence and distribution of second phases, and the processing conditions [36–45]. There are several reviews and overviews focused on the impact of deformation processing and deformation features on the corrosion behaviour of Mg-based alloys [34,46–50]. In general, the grain refinement produced by SPD processing leads to a uniform corrosion due to the increase in grain boundary numbers which improves the corrosion properties of Mg-based alloys. In practice, in many cases it is found that improving the strength and formability of the Mg–RE alloys have a negative effect on the corrosion performance [15,51–53]. The increase in dislocation density and the presence of twins appear to decrease the corrosion resistance of deformed Mg-based alloys [49]. However, different investigations have shown contradictory results because the deformation features may be beneficial for decreasing the corrosion rate of Mg-based alloys [48,49,54,55].

Nevertheless, it is concluded that HPT processing generates a non-equilibrium ultrafine microstructure due to the introduction of high densities of dislocations and vacancies and this causes a loss of the excellent mechanical properties during the recovery and grain growth processes [56,57]. Furthermore, although HPT processing has been widely reported in Mg-based alloys, research dealing with the thermal stability and the overall impact on the corrosion behaviour remains extremely limited [58–63].

The present research was initiated to compare the evolution of deformation and recrystallisation microstructure and texture of three low RE containing Mg–RE alloys, with LREE represented by Mg-1.4Nd (wt.%) alloy and HREE represented by Mg-0.6Gd and Mg-0.4Dy (wt.%) alloys. Furthermore, the corrosion performance of these Mg–RE alloys in a 3.5% NaCl (wt.%) solution was correlated with the effect of the RE solute elements and the changes in the deformation and recrystallisation microstructures.

Principally, the choice of 1.4% Nd, 0.6% Gd, and 0.4% Dy was based on the phase diagram to obtain single-phase Mg–RE alloys (only Mg matrix) [64]. In addition to the single-phase purpose, the low content of (0.6% for Gd element) and (0.4% for Dy element) was chosen due to the high cost of HREE.

The present study is part of a series of investigations that have focussed on the evolution of microstructure and corrosion performance in various binary Mg–RE alloys with low RE containing. First, the evolution of microstructure and texture were evaluated during deformation processing and subsequent annealing of Mg-1.4Nd (wt.%) [59] and Mg-0.4Dy (wt.%) [8,9,43,58] alloys. Thereafter, the effect of RE (RE = Ce, Nd, La, Gd, and

Dy) elements on the corrosion behaviours was investigated for the as-cast state of Mg–RE alloys [13] and the effect of a homogenous treatment on the corrosion behaviour was investigated using Mg-1.4Ce and Mg-1.4Nd (wt.%) alloys [65]. The present research was undertaken to extend the understanding of the effect of each RE elements on the Mg-based alloys and especially to contribute towards controlling the design of these alloys.

2. Materials and Experimental Procedures

2.1. Materials

The as-cast Mg–RE alloys used in this study were Mg-1.4Nd, Mg-0.6Gd, and Mg-0.4Dy (% wt.), generously provided by the Institute für Metallkunde und Metallphysik, Aachen, Germany. The alloys were fabricated by induction melting and casting using a preheated copper mould under a protective gas atmosphere of Ar/CO_2. Then, the as-cast alloys were heat treated at 420 °C for 20 h.

As noted earlier, the initial microstructures of these three Mg–RE alloys were characterised by typical as-cast microstructures mostly in the form of coarse grains with the presence of second phases $Mg_{12}Nd$, $Mg_{24}Nd$, and $Mg_{41}Nd_5$ in Mg-1.4Nd alloy, $Mg_{12}Gd$ in Mg-0.6Gd alloy, and $Mg_{24}Dy_5$ in Mg-0.4Dy alloy [13,58]. The Mg–RE discs with 10 mm diameters and 0.85 mm thicknesses were processed by HPT at RT through 5 turns as illustrated in Figure 1 with a 1 rpm rotational speed using an imposed applied pressure of 6.0 GPa under quasi-constrained conditions [66]. Thereafter, the HPT-processed samples were annealed in a radiation furnace for 1 h at 250 or 450 °C.
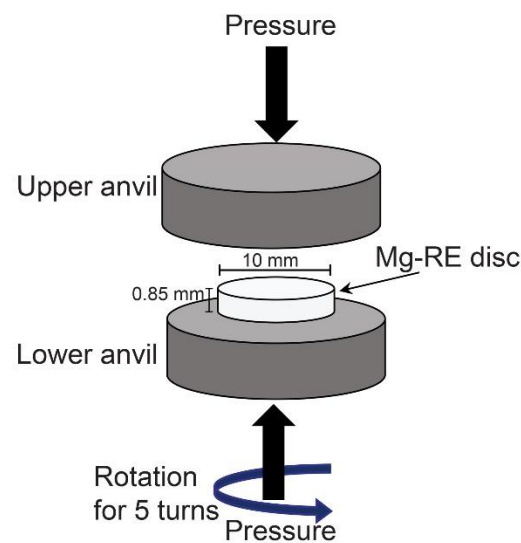

Figure 1. Schematic illustration showing the HPT processing.

2.2. Microstructure and Texture Characterisation

The microstructures and textures of the HPT-processed and annealed samples were investigated near the centres of the rotation direction-shear direction (RD-SD) plane (designated the shear plane (SP)) of the discs using EBSD after surface preparation consisting of grinding with progressively finer SiC papers, followed by mechanical polishing using a diamond solution with particle sizes down to 0.25 μm, and finished by ionic polishing using a Gatan PECS II system at a high voltage of 5 kV for 15 min.

The observations were carried out using a scanning electron microscope (FEG-SEM SUPRA 55 VP) operating at 20 kV. The scanned areas were 100×100 μm² with a 0.1 μm step size for samples HPT-processed and annealed at 250 °C and 800×800 μm² with a 1 μm step size for HPT samples annealed at 450 °C. The TSL Orientation Imaging Microscopy (OIM) software was used for the acquisition and analysis of the EBSD data. Spurious boundaries with misorientation angles lower than 2° were omitted to avoid any orientation noise. The grain boundary types are separated into very low-angle grain boundaries (VLAGBs) with

misorientations 2°< θ < 5°, low-angle grain boundaries (LAGBs) with 5°< θ < 15°, and high-angle grain boundaries (HAGBs) with θ > 15°, respectively. The fraction of recrystallisation was calculated using the grain orientation spread (GOS) approach where grains with GOS values lower than 1° were considered fully recrystallised [67]. The deformation and recrystallisation textures were evaluated by MATLAB toolbox MTEX [68].

2.3. Electrochemical Tests

Electrochemical tests were conducted in a 3.5% NaCl solution at room temperature using an AUTOLAB PGSTAT302N potentiostat. A standard three-electrode cell was used, where Mg–RE samples of 0.385 cm^2 were the working electrode, a platinum plate was the counter electrode, and a saturated calomel electrode (SCE) was the reference electrode. Before the electrochemical test, the surfaces of the samples were ground with progressively finer SiC papers followed by a cleaning with acetone. The open-circuit potential was measured for at least 90 min for all samples. Then, electrochemical impedance spectroscopy tests were performed with an amplitude of 10 mV in the frequency range from 10^5 Hz to 10^{-2} Hz. Finally, the polarisation curves were recorded with a scan rate of 2 mV.s^{-1}. At least three replicated tests were achieved for each sample to ensure reproducibility.

3. Results

3.1. Microstructure and Texture Evolution

Figure 2 shows the orientation imaging microscopy (OIM) images in the inverse pole figure (SPN-IPF) maps and grain size distributions of the HPT-processed and annealed Mg-1.4Nd, Mg-0.6Gd, and Mg-0.4Dy alloys at 250 and 450 °C for 1 h, respectively, where SPN denotes the shear plan normal direction. Figure 3 shows the average grain size and the recrystallisation fraction of the HPT-processed and annealed Mg–RE samples.

It is readily apparent that the deformation microstructure of the Mg-1.4Nd alloy is heterogonous with large deformed grains surrounded by small dynamically recrystallised grains leading to a mean grain size of ~2.0 μm (Figure 2a). By contrast, the HPT-processed Mg-0.6Gd and Mg-0.4Dy alloys exhibit a similar homogenous microstructure formed principally of fine dynamically recrystallised grains (Figure 2b,c). The mean grain size for the HPT-processed Mg-0.6Gd and Mg-0.4Dy samples were ~1.0 and ~1.2 μm, respectively. Figure 3 indicates that the DRX fraction in the HPT-processed Mg-1.4Nd alloy (20.2%) is remarkably low by comparison with the HPT-processed Mg-0.6Gd (55.8%) and Mg-0.4Dy (51.9%) alloys.

Figure 2d shows that the microstructure of the Mg-1.4Nd alloy remains heterogenous after annealing at 250 °C for 1 h with a mean grain size of ~1.5 μm and a slight increase in the recrystallisation fraction (35.9%). Annealing at 250 °C led to an increase in grain size for the Mg-0.6Gd and Mg-0.4Dy samples to ~1.2 and ~3.3 μm and an increase in the recrystallisation fraction to 70 and 90%, respectively. The microstructure of the Mg-1.4Nd sample became homogenous and fully recrystallised with a mean grain size of ~37.8 μm after annealing at 450 °C for 1 h as shown in Figure 2g. By contrast, the microstructures of the annealed Mg-0.6Gd (Figure 2h) and Mg-0.4Dy (Figure 2i) alloys at 450 °C for 1 h showed the presence of small and large recrystallised grains where this bimodal grain distribution is more obvious in the Mg-0.4Dy sample. The resulting mean grain size of the Mg-0.4Dy alloy (~15.5 μm) was lower than for the Mg-0.6Gd alloy (~20.1 μm).

The histograms of the grain boundary misorientations are shown in Figure 4 for the HPT-processed and annealed Mg-1.4Nd, Mg-0.6Gd, and Mg-0.4Dy alloys at 250 and 450 °C for 1 h, respectively. These grain boundary misorientation angle distributions are far from the random distribution for all Mg–RE samples. A distinct change in the grain boundary distribution is noticeable in the Mg-1.4Nd alloy after annealing at 450 °C whereas the grain boundary distributions were similar for the Mg-0.6Gd and Mg-Mg-0.4Dy alloy throughout the HPT processing and annealing treatments. Both the deformed and annealed alloys exhibited a peak maximum of around 30°, indicating the development of a 30° <0001>

misorientation relationship which is commonly observed during growth of recrystallised grains in hexagonal alloys [69–71].
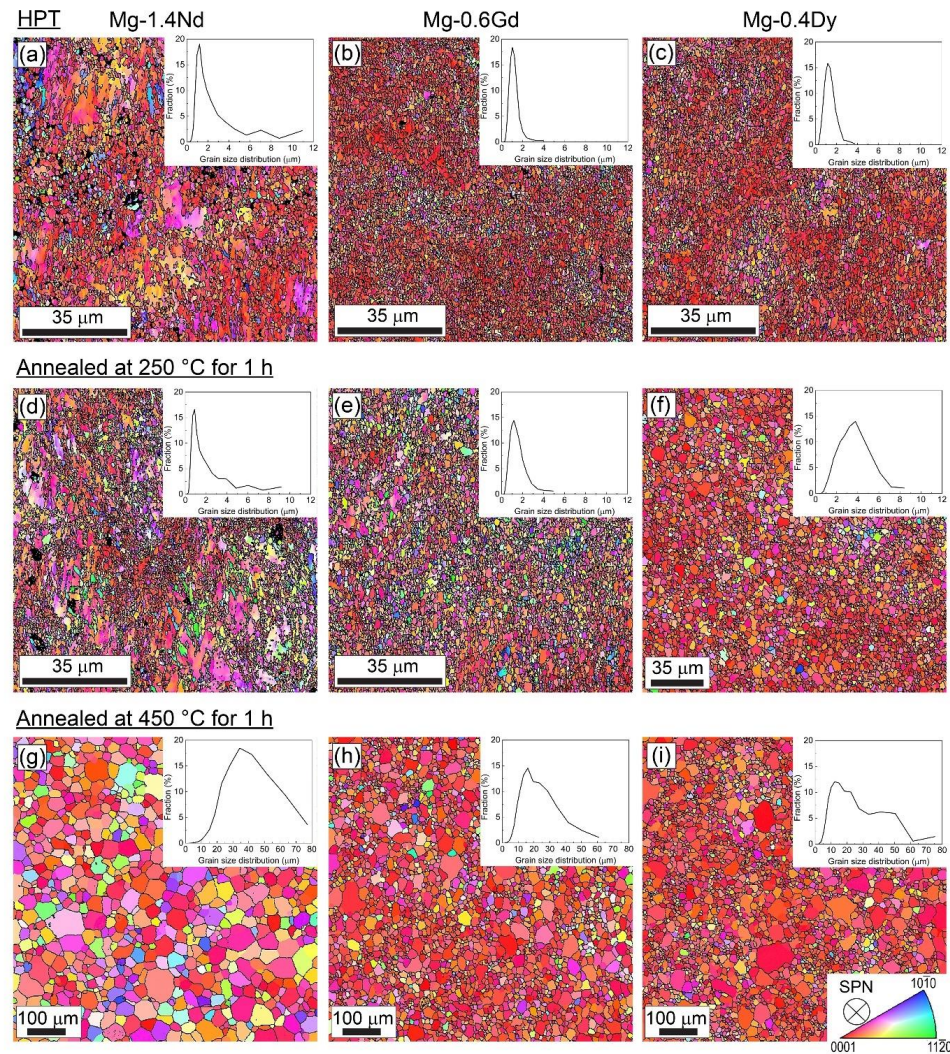
Figure 2. SPN-IPF maps and grain size distributions of HPT-processed: (**a**) Mg-1.4Nd, (**b**) Mg-0.6Gd, (**c**) Mg-0.4Dy, annealed at 250 °C for 1 h: (**d**) Mg-1.4Nd, (**e**) Mg-0.6Gd, (**f**) Mg-0.4Dy and annealed at 450 °C for 1 h: (**g**) Mg-1.4Nd, (**h**) Mg-0.6Gd, and (**i**) Mg-0.4Dy alloys. The HAGBs are indicated by a black line. SPN denotes the shear plane normal direction.
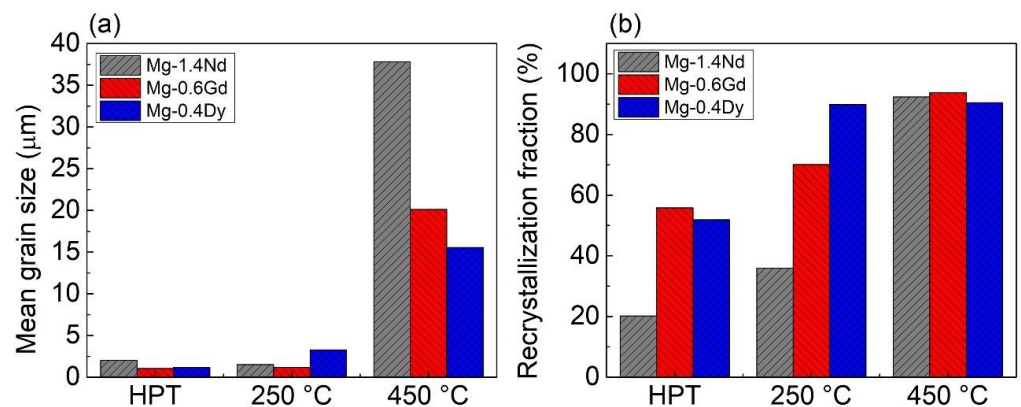
Figure 3. Evolution of: (**a**) mean grain size and (**b**) recrystallisation fraction of HPT-processed and annealed Mg-1.4Nd, Mg-0.6Gd, and Mg-0.4Dy alloys at 250 and 450 °C for 1 h, respectively.
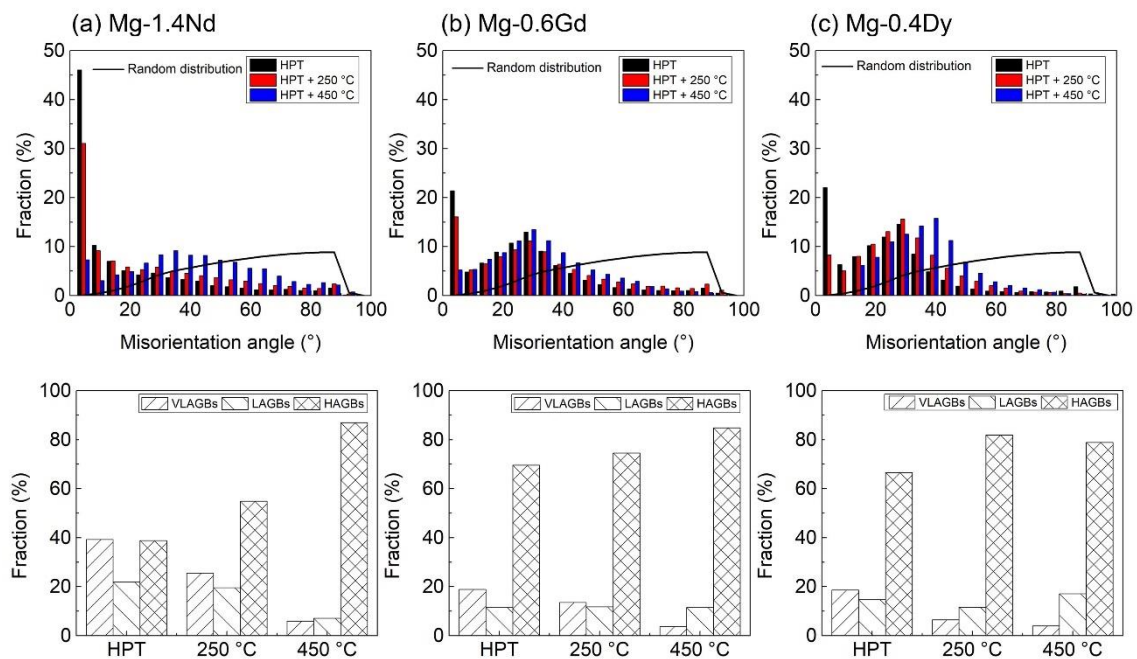
Figure 4. Grain boundary misorientation angle distributions and fractions of VLAGBs, LAGBs, and HAGBs of samples HPT-processed and annealed at 250 and 450 °C for 1 h: (**a**) Mg-1.4Nd, (**b**) Mg-0.6Gd, and (**c**) Mg-0.4Dy alloys.

The evolutions of the VLAGBs, LAGBs, and HAGBs fractions of the HPT-processed and annealed Mg–RE alloys are shown in Figure 4. The fractions of VLAGBs (39.3%) and HAGBs (38.8%) are very similar in the HPT-processed Mg-1.4Nd sample. However, the fraction of VLAGBs drastically decreases and the fraction of HAGBs increases with increasing annealing temperature owing to static recrystallisation and the formation of new grains to reach a value of 6% and 87% at 450 °C, respectively. By contrast, the HAGBs fraction dominates in the HPT-processed Mg-0.6Gd (69.6%) and Mg-0.4Dy (66.6%) samples due to the occurrence of DRX during the HPT processing. The fraction of HAGBs increases slightly with the annealing treatments and reached a value of 85% for the Mg-0.6Gd alloy and 79% for the Mg-0.4Dy alloy after annealing at 450 °C. It is interesting to note that the fraction of LAGBs decreases with increasing annealing temperature for the Mg-1.4Nd alloy while its fraction seems stable (around 11%) through the HPT processing and annealing treatments in the Mg-0.6Gd and Mg-0.4Dy alloys.

Figure 5 presents the SEM photos in the backscattering mode with analysed points (1–9) in atomic percentage obtained by EDS for the HPT-processed and annealed Mg-1.4Nd, Mg-0.6Gd, and Mg-0.4Dy alloys at 250 and 450 °C for 1 h, respectively. The three alloys under deformation and annealing conditions show the presence of small second phases as is evident from the zoomed areas (yellow boxes) of the SEM photos. As can be observed from Figure 5a, the HPT-processed Mg-1.4Nd alloy contains three kinds of particles given by $Mg_{41}Nd_5$ (point 1), $Mg_{12}Nd$ (point 2), and $Mg_{24}Nd$ (point 3).

The EDS analysis of HPT-processed Mg-0.6Gd sample shows also the presence of three types of particles: the atomic percentage of Mg and Gd of the point 4 allows the identification of the particle as the Mg_5Gd phase [72]. By contrast, points 5 and 6 indicate the presence of particles with low (4.0%) and high atomic fractions (67.5%) of Gd, respectively. The EDS analysis of the HPT-processed Mg-0.4Dy sample shows the presence of $Mg_{24}Dy_5$ second phase (point 7) and particles with a low fraction of Dy (points 8 and 9). The development of particles without knowing their stochiometry (points 5 and 6) in the Mg-0.6Gd alloy and points (8 and 9) in the Mg-0.4Dy alloy are probably due to the fragmentation during HPT processing of the initial Mg_5Gd and $Mg_{24}Dy_5$ second phases [13], respectively. The presence of Si element in different points in Mg-0.6Gd and Mg-0.4Dy alloys is due to grinding with SiC papers during the sample preparation. It is apparent from Figure 5

that the amount of the second phases in Mg-1.4Nd samples is much higher than in the Mg-0.6Gd and Mg-0.4Dy samples and their distributions change after annealing treatments as is evident by the magnification of the yellow boxes of the annealed Mg-1.4Nd samples (Figure 5d,g) because of the development of precipitation phenomena [59,73]. It is well known that precipitation occurs in the supersaturated solid solution (SSS) Mg–Nd alloy during the annealing temperature range of 150–450 °C and can follow the sequence [73]:

$$SSS \rightarrow GP\ zone \rightarrow \beta'' \rightarrow \beta' \rightarrow \beta_1 \rightarrow \beta\ (Mg_{12}Nd) \rightarrow \beta_e(Mg_{41}Nd_5) \tag{1}$$

at (%)	Mg	Nd
1	88.3	11.7
2	91.8	8.2
3	95.9	4.1

at (%)	Mg	Gd	Si
4	85.2	10.2	4.6
5	94.8	4	1.2
6	32.5	67.5	-

| at (%)	Mg	Dy	Si
7	72.5	13.5	14.0
8	90.5	7.3	2.2
9	95.3	2.5	2.2
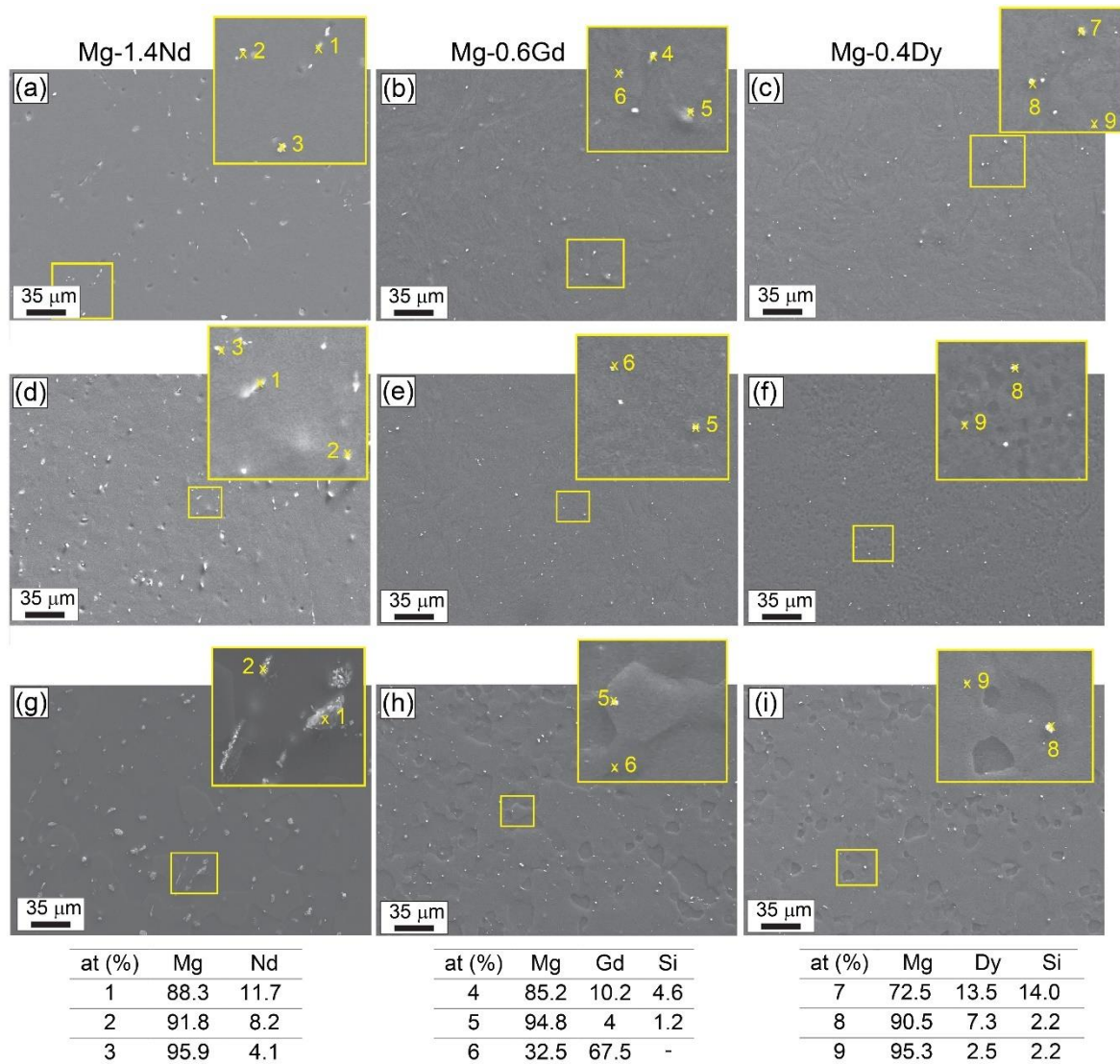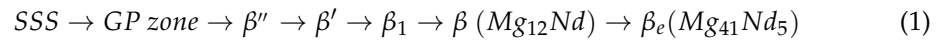
Figure 5. SEM photos of HPT-processed: (**a**) Mg-1.4Nd, (**b**) Mg-0.6Gd, (**c**) Mg-0.4Dy, annealed at 250 °C for 1 h: (**d**) Mg-1.4Nd, (**e**) Mg-0.6Gd, (**f**) Mg-0.4Dy and annealed at 450 °C for 1 h: (**g**) Mg-1.4Nd, (**h**) Mg-0.6Gd, and (**i**) Mg-0.4Dy alloys.

In contrast, Figure 5e–i demonstrated that the size, the nature (points 5 and 6 for Mg-0.6Gd alloy and points 8 and 9 for Mg-0.6Dy alloy), and the distribution of the second phases in both the Mg-0.6Gd and Mg-0.4Dy samples are stable through the annealing conditions.

The texture evolution of the HPT-processed and annealed Mg-1.4Nd, Mg-0.6Gd, and Mg-0.4Dy alloys at 250 and 450 °C for 1 h are shown in Figure 6, respectively. The recalculated {0002} pole figure of the HPT-processed Mg-1.4Nd sample shown in Figure 6a indicates the development of a typical basal texture where the basal (0002) planes are

parallel to the shear plane but slightly shifted towards SD. This shift of the basal texture towards SD increases after annealing at 250 °C for 1 h (Figure 6d). It is interesting to note that annealing at 450 °C for 1 h causes a weakening of the texture (4.2 multiples random of distribution (mrd) versus 10 mrd in the case of the HPT-processed sample) as shown in Figure 6g.
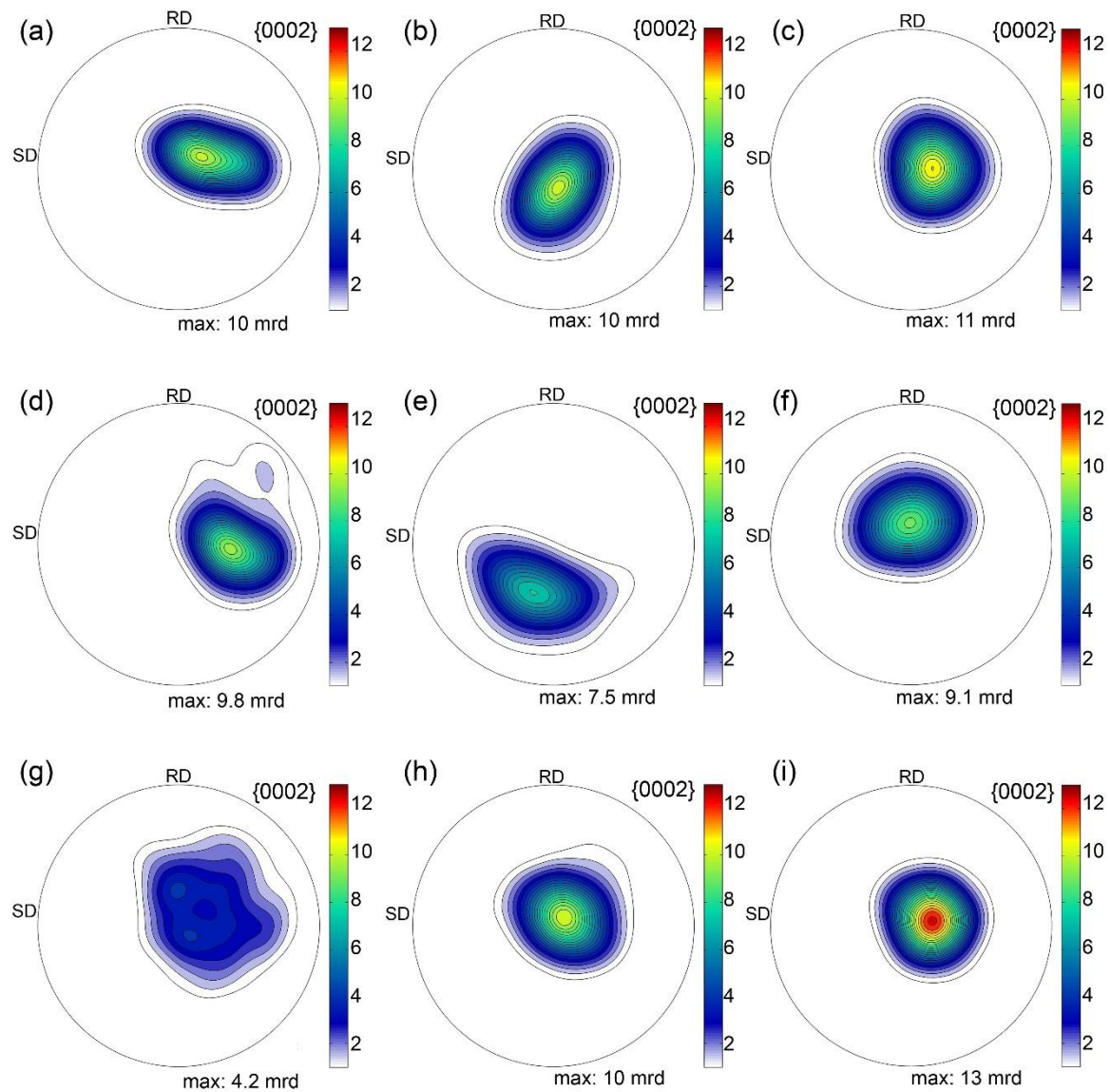

Figure 6. Evolution of texture presented by the recalculated {0002} pole figures of the HPT-processed: (**a**) Mg-1.4Nd, (**b**) Mg-0.6Gd, (**c**) Mg-0.4Dy, annealed at 250 °C for 1 h: (**d**) Mg-1.4Nd, (**e**) Mg-0.6Gd, (**f**) Mg-0.4Dy and annealed at 450 °C for 1 h: (**g**) Mg-1.4Nd, (**h**) Mg-0.6Gd, and (**i**) Mg-0.4Dy alloys.

Figure 6b,e,h show that the basal texture developed during HPT processing of the Mg-0.6Gd alloy shifts towards RD during annealing at 250 °C for 1 h whereas annealing at 450 °C for 1 h keeps the basal texture already formed during the HPT processing. For the Mg-0.4Dy alloy, the basal texture appears stable through the deformation and annealing conditions as can be seen from Figure 6c,f,i.

3.2. Electrochemical Corrosion Behaviour

Figure 7 illustrates the potentiodynamic polarisation curves of the HPT-processed and annealed Mg-1.4Nd, Mg-0.6Gd, and Mg-0.6Dy samples in a 3.5% NaCl solution. It is obvious that the anodic and cathodic branches of all samples are unsymmetrical.
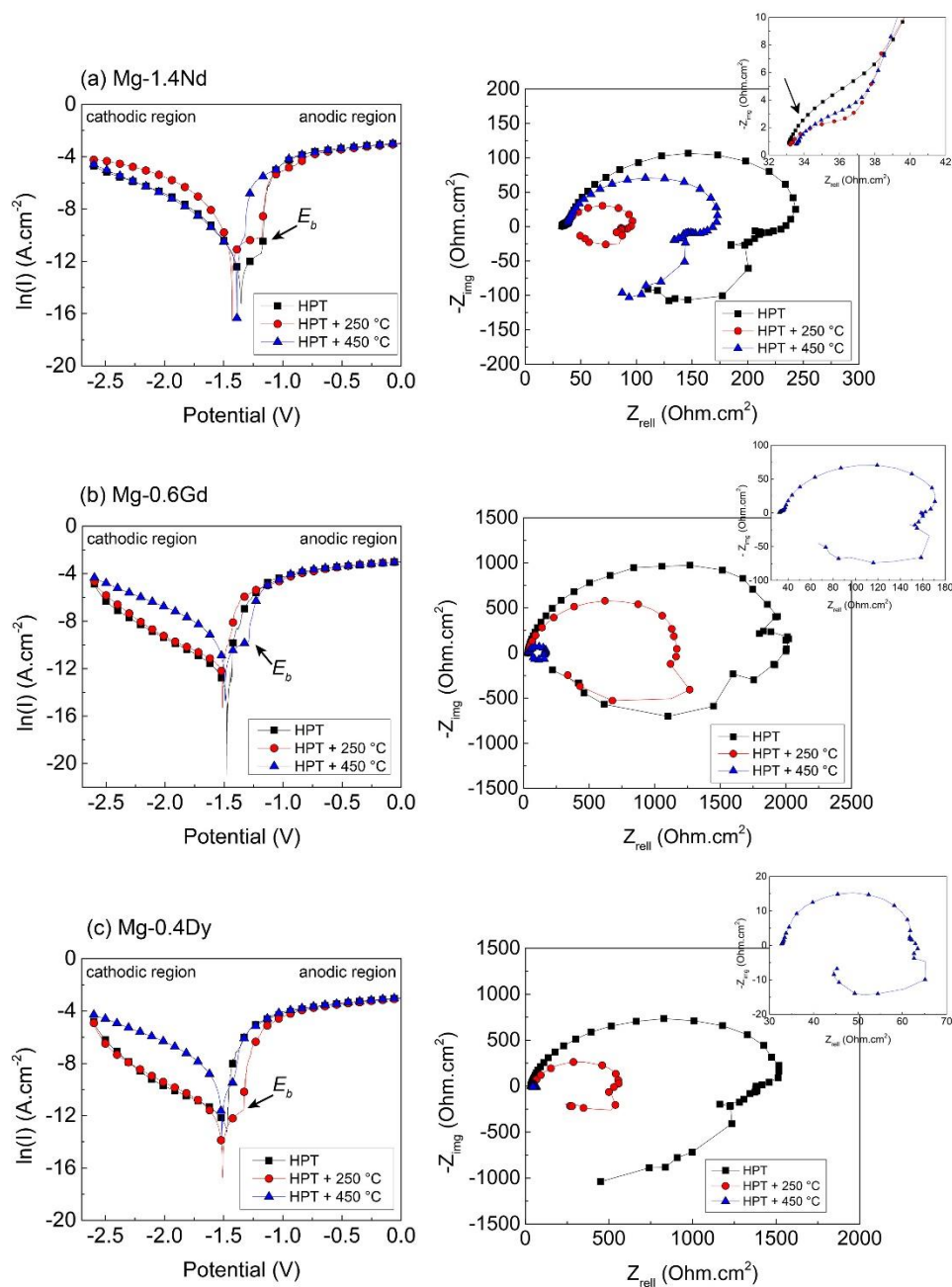
Figure 7. Polarisation curves and Nyquist plots in a 3.5% NaCl solution of deformed and recrystallised samples of: (**a**) Mg-1.4Nd, (**b**) Mg-0.6Gd, and (**c**) Mg-0.4Dy alloys. The Nyquist plots of the HPT-processed and annealed Mg-1.4Nd (250 and 450 °C), annealed Mg-0.6Gd at 450 °C, and Mg-0.4Dy at 450 °C are placed at the upper right with a small scale for further visibility.

Generally, the anodic and the cathodic branches in the polarisation curve represent the anodic dissolution of the Mg metal and the cathodic hydrogen evolution reaction, respectively [74]:

$$\text{Anodic reaction: } Mg \rightarrow Mg^{2+} + 2e^- \tag{2}$$

$$\text{Cathodic reaction: } 2H_2O + 2e^- \rightarrow 2OH^- + H_2\uparrow \tag{3}$$
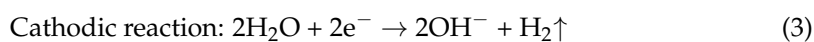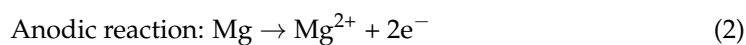
It is noted that the cathodic reaction kinetics are similar for the HPT-processed and annealed Mg-1.4Nd at 450 °C and they increase for the annealed sample at 250 °C. For the Mg-0.6Gd and Mg-0.4Dy alloys, the cathodic kinetics are similar for the HPT-processed and

annealed at 250 °C samples and they increase when the samples are annealed at 450 °C for 1 h. A film breakdown potential, E_b, appears on the anodic branch of the HPT-processed Mg-1.4Nd ($E_b = -1.18$ V_{SCE}) and annealed Mg-1.4Nd at 250 °C ($E_b = -1.17$ V_{SCE}), annealed Mg-0.6Gd at 450 °C ($E_b = -1.28$ V_{SCE}), and annealed Mg-0.4Dy at 250 °C ($E_b = -1.33$ V_{SCE}), demonstrating a tendency for localised corrosion. The anodic branch of the majority of the Mg–RE samples does not show a linear Tafel region, probably due to the negative difference effect [75,76]. This feature is usually observed in Mg-based alloys and it results from the strong hydrogen evolution during the recording of the corrosion current density–potential curves [75,76]. In contrast, an extended linear Tafel region occurred in each cathodic branch, suggesting a relatively uniform hydrogen evolution and a constant corrosion rate. Hence, the corrosion potential, E_{corr}, and the corrosion current density, I_{corr}, are fitted from the cathodic polarisation curves. The values of E_{corr}, I_{corr}, and the cathodic slope β_c values of the Mg–RE samples are listed in Table 1.

Table 1. E_{corr}, I_{corr}, and β_c fitted from the polarisation curves of Mg–RE samples.

|	E_{corr} (V_{SCE})	I_{corr} (A.cm^{-2})	β_c (V_{SCE})
Mg-1.4Nd			
HPT	−1.35	1.07×10^{-4}	−0.32
HPT + 250 °C	−1.42	5.93×10^{-4}	−0.30
HPT + 450 °C	−1.36	1.01×10^{-4}	−0.20
Mg-0.6Gd			
HPT	−1.47	5.18×10^{-6}	−0.19
HPT + 250 °C	−1.48	9.45×10^{-6}	−0.21
HPT + 450 °C	−1.51	1.55×10^{-4}	−0.25
Mg-0.4Dy			
HPT	−1.47	6.39×10^{-6}	−0.21
HPT + 250 °C	−1.51	8.81×10^{-6}	−0.22
HPT + 450 °C	−1.52	3.29×10^{-4}	−0.29

Table 1 shows that the range of E_{corr} is quite similar for the three Mg–RE alloys, especially for the Mg-0.6Gd and Mg-0.4Dy alloys, and it does not vary much with the annealing conditions. However, a net increase in the I_{corr} values can be visualised as a function of annealing conditions, indicating a decline of the corrosion resistance of the three HPT-processed Mg–RE alloys with the heat treatments mainly during annealing at 450 °C for 1 h.

Figure 7 shows also the Nyquist plots in a 3.5% NaCl solution of HPT-processed and annealed Mg-1.4Nd, Mg-0.6Gd, and Mg-0.4Dy alloys. The Nyquist plots of the HPT-processed and annealed Mg-1.4Nd (250 and 450 °C), annealed Mg-0.6Gd at 450 °C, and Mg-0.4Dy at 450 °C are placed at the upper right with a small scale for further visibility. As can be seen, the three Mg–RE alloys under thermomechanical processing exhibit the same shape of the Nyquist curve consisting of one visible capacitive loop at the high-frequency region and two inductive loops in the low and medium frequency regions signifying a similar corrosion mechanism. However, the upper right plot with a smaller scale demonstrates that the Mg-1.4Nd samples developed a very small capacitive loop which was almost indistinguishable at the high-frequency region. This observation is also evident for the Mg-0.6Gd and Mg-0.4Dy samples. The Nyquist plots show that the diameter of the loops changes with the thermomechanical processing indicating different corrosion rates.

It is well known that the formation of a capacitive loop in the high-frequency region is attributed to the charge transfer resistance and formation of a double layer at the interface between the metal and the solution [77]. The presence of a capacitive loop in the medium-frequency region is due to the formation of the corrosion product layer and its resistance whereas the presence of an inductance loop is characteristic of pitting corrosion and dissolution of the protective film [78]. In addition, the inductive loop reflects the

presence of metastable Mg^+ during the dissolution of the Mg metal and/or the relaxation of surface-adsorbed species such as $Mg (OH)^+$ and $Mg(OH)_2$ [13,78,79].

Usually, the Nyquist data are fitted by a simulated equivalent circuit to explain the general corrosion process and the corresponding mechanism. Therefore, the equivalent electrical circuit and the fitted data of the Nyquist curves of the HPT-processed and annealed Mg–RE samples are presented in Figure 8 and Table 2, respectively.
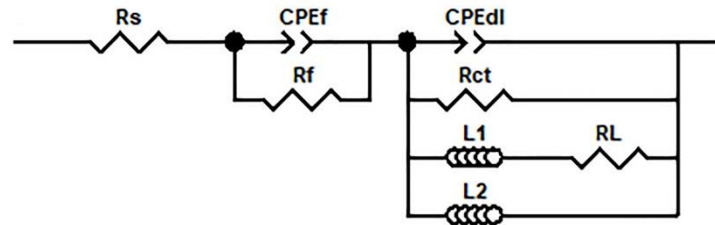
Figure 8. Equivalent electric circuit used to fit the Nyquist plots of HPT-processed and annealed Mg–RE samples.

Table 2. Electrochemical parameters obtained from the fits of the experimental Nyquist plots of Mg–RE samples.

	R_s ($\Omega.cm^2$)	CPE_f ($F.cm^{-2}$)		R_f ($\Omega.cm^2$)	CPE_{dl} ($F.cm^{-2}$)		R_{ct} ($\Omega.cm^2$)	L_1 ($H.cm^{-2}$)	R_L ($\Omega.cm^2$)	L_2 ($F.cm^{-2}$)	R_p ($\Omega.cm^2$)
		Y_f	n_f		Y_{dl}	n_{dl}					
Mg-1.4Nd											
HPT	32.96	1.38×10^{-5}	0.97	4.95	6.14×10^{-5}	0.91	251.4	23.85	581.4	1198	213.4
HPT + 250 °C	31.61	3.35×10^{-3}	0.39	10.04	1.23×10^{-4}	0.97	61.2	9.32	183.2	263.2	87.5
HPT + 450 °C	33.33	1.74×10^{-5}	0.95	3.81	8.75×10^{-5}	0.92	162.6	19.06	368.1	770.2	149.9
Mg-0.6Gd											
HPT	32.95	2.49×10^{-5}	0.98	504.2	4.55×10^{-4}	0.85	3825	79.34	2340	6270	1988
HPT + 250 °C	34.06	3.49×10^{-3}	0.87	244.4	2.29×10^{-5}	0.89	1379	21.32	1205	3189	921.5
HPT + 450 °C	30.47	4.29×10^{-3}	0.37	11.31	7.98×10^{-5}	0.96	150.8	22.77	664.8	747	164.7
Mg-0.4Dy											
HPT	33.04	1.19×10^{-4}	0.98	1.75	1.88×10^{-5}	0.91	1713	595.1	6017	9975	1368.1
HPT + 250 °C	32.65	4.34×10^{-4}	0.61	75.8	3.64×10^{-5}	0.97	527.5	103.6	3955	1653	573.9
HPT + 450 °C	32.76	3.89×10^{-3}	0.90	8.51	3.78×10^{-4}	0.92	34.92	3.69	169.8	86.86	70.2

In these equivalent circuits, R_s, R_{ct}, R_f, and R_L present the solution resistance, charge transfer resistance, film resistance, and inductance resistance, respectively, and CPE_{dl} and CPE_f are constant phase elements representing the capacitive loops in the high and medium frequencies regions, respectively. The *CPE* is defined by two values, *Y* and *n*, and it is used instead of the capacitor in the case of a non-homogeneity of the sample surface [80]. When $n = 1$, *CPE* is equal to a capacitor.

Table 2 shows that the three Mg–RE alloys under the deformation and annealing conditions have almost the same R_s value indicating that the Nd, Gd, and Dy alloying elements have similar behaviour in contact with the 3.5% NaCl solution.

The double-layer capacitance Y_{dl} of the Mg–RE alloys changes with the thermomechanical conditions. Basically, the double-layer capacitance decreases with increasing the surface of the protective film [81]. In general, Table 2 shows that the Y_{dl} values increase with the annealing treatment of the three alloys indicating a decrease in the protective film surface except for the Mg-0.6Gd alloy.

The R_{ct} value is proportional to the dissolution rate of the Mg metal. Based on this, the corrosion rate of the Mg–RE alloys increases with annealing treatments except for the Mg-1.4Nd alloy where the R_{ct} of the sample annealed at 450 °C ($R_{ct} = 162.6 \ \Omega.cm^2$) is higher than for the sample annealed at 250 °C ($R_{ct} = 61.2 \ \Omega.cm^2$). The HPT-processed Mg-0.6Gd sample exhibits a lower corrosion rate ($R_{ct} = 3825 \ \Omega.cm^2$) and the annealed Mg-0.4Dy at 450 °C sample shows a higher corrosion rate ($R_{ct} = 34.9 \ \Omega.cm^2$).

The film capacitance Y_f of the HPT-processed Mg-1.4Nd sample increases after annealing at 250 °C and then decreases during annealing at 450 °C, while the Y_f values of the HPT-processed Mg-0.6Gd and Mg-0.4Dy samples increase gradually with annealing temperatures. The values of n_{dl} and n_f are close to 1 demonstrating that the capacitive loops are well defined, except for the annealed Mg-1.4Nd and Mg-0.4Dy samples at 250 °C where n_f = 0.39 and 0.61, respectively.

The values of the inductions (L_1 and L_2) of the HPT-processed Mg–RE alloys decrease with the annealing temperature indicating that the corrosion pits became more severe with the occurrence of static recrystallisation.

The corrosion resistance, R_p, of the Mg–RE samples shown in Table 2 was estimated based on the values of different resistances present in the equivalent circuit [82]:

$$R_p = R_s + R_f + \frac{R_{ct} R_L}{R_{ct} + R_L} \tag{4}$$

As is noted, the corrosion resistance of the HPT-processed Mg-0.6Gd and Mg-0.4Dy samples significantly decreases with increasing annealing temperature whereas the corrosion resistance of the HPT-processed Mg-1.4Nd sample decreases after annealing at 250 °C and becomes better after annealing at 450 °C. These tendencies are in good agreement with the evolution of potentiodynamic polarisation curves.

4. Discussion

4.1. Microstructure and Texture Evolution

As shown in Figures 2 and 3, HPT processing at the same equivalent stain (five HPT turns) results in different microstructures for the LREE Mg-1.4Nd alloy compared with the HREE Mg-0.6Gd and Mg-0.4Dy alloys. The grain refinement and the homogenous microstructure observed in the HPT-processed Mg-0.6Gd and Mg-0.4Dy samples are mainly attributed to the occurrence of extensive DRX, while the DRX was extremely retarded in the HPT-processed Mg-1.4Nd sample which resulted in a heterogeneous deformation microstructure. The heterogeneous microstructure remained present in the Mg-1.4Nd alloy even after annealing at 250 °C for 1 h. Apparently, a good thermal stability is obtained for the three Mg–RE alloys during annealing at 250 °C for 1 h, except for an increase in the recrystallisation fraction of the Mg-0.6Gd and Mg-0.4Dy alloys (as shown in Figure 3).

The restriction of the DRX process in Mg-1.4Nd alloy shown in Figure 2a,d allows the identification of interesting deformation features and some DRX mechanisms. As an example, Figure 9 shows SPN-IPF and GOS maps highlighted with VLAGBs (marked in white lines), LAGBs (blue lines), HAGBs (black lines), and extension twin 86° <11–20> (yellow lines) of typical deformation zones taken from the HPT-processed and annealed Mg-1.4Nd at 250 °C samples (Figure 2a,d).

First, these microstructures show the presence of an extension twin 86° <11–20> and the magnified IPF of the extension twins (black box) in both samples shows that they contain a very small number of VLAGBs. The restriction of sub-grain boundaries within the twins indicates an absence of the twin-induced dynamic recrystallisation (TDRX) mechanism [83]. However, some twins became thicker during the annealing treatment at 250 °C as shown by white arrows in the GOS map (Figure 9d). The presence of an extension twin creates new orientations as demonstrated by the corresponding {0002} pole figure between the parent grain (PG) and the extension twin (ET) shown in Figure 9e,f. This may be one of the reasons for the weakening of texture as a function of the annealing conditions for the Mg-1.4Nd alloy as shown in Figure 6d,g.

Second, Figure 9g,h depict the presence of the sub-grain development (SGD) mechanism in both samples. The high magnifications of the green boxes in both IPF maps show the formation of fine DRX grains within the deformed grains by the accumulation of dislocations and their gradual transformation from VLAGBs to LAGBs and then to HAGBS to thereby form new grain [84]. Again, the annealing treatment at 250 °C of the HPT-processed Mg-1.4Nd sample is not sufficient to develop a complete recrystallisation

microstructure from this mechanism. Concerning the texture evolution, it must be noted that the orientations of recrystallised grains generated by the SGD mechanism shown in Figure 9g,h are very different from each other (see grains G_1, G_2, G_3, and G_4) and from the deformed grains (see G_{d1} and G_{d2}) as well. This is another reason for the texture weakening of the Mg-1.4Nd alloy as a function of the annealing conditions.
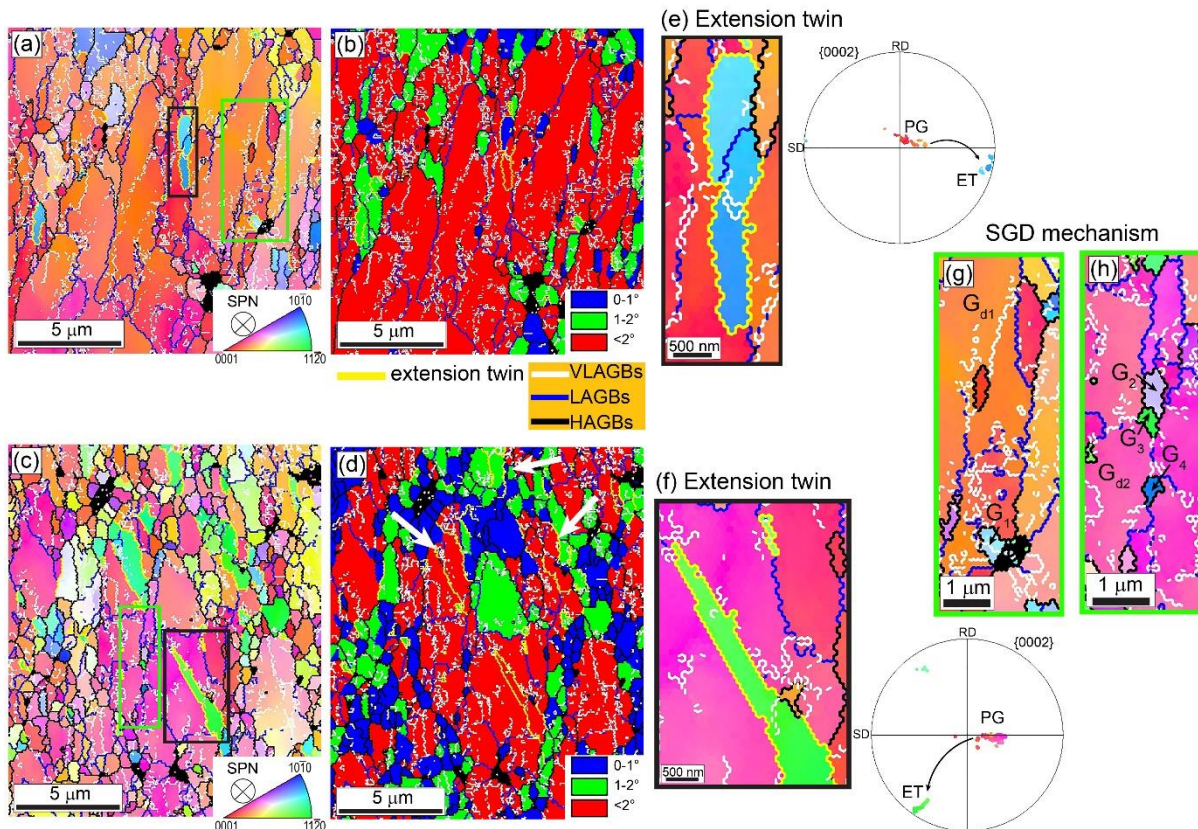
Figure 9. IPF and GOS maps of selected regions from the microstructures of: (**a,b**) HPT-processed (from Figure 2) and (**c,d**) annealed Mg-1.4Nd at 250 °C for 1 h (from Figure 2) showing the presence of (**e,f**) an extension twin (black box) and corresponding {0002} pole figure and (**g,h**) a sub-grain development mechanism (green box).

It is advantageous that the light Nd element can strongly change the recovery process of the Mg matrix rather than the heavy Gd and/or Dy elements. The incomplete TDRX and SGD mechanisms are caused by the restriction on the advent of dynamic recovery. This leads to the conclusion that the Nd element has more effect in reducing the stacking fault energy of the Mg solid solution resulting in a stabilisation of the dislocation configuration and an inhibition of dislocation movement [10,85]. In addition, the pinning effect of the second phase prevents the transformation of dislocations into HAGBs. As shown in Figure 5, the microstructure of the Mg-1.4Nd alloy contains a higher fraction of second particles than the Mg-0.6Gd and Mg-0.4Dy alloys. On the one hand, the solubility of the Nd element in the Mg matrix is very low with a value of 3.6% at the eutectic temperature [64]. In the studied Mg-1.4Nd alloy with 1.4% of Nd element, the presence of $Mg_{41}Nd_5$ or $Mg_{12}Nd$ phases was found in the as-cast and deformation microstructures and their precipitation during the used annealing treatment is expected [64]. On the other hand, the presence of second phases in the Mg-0.6Gd and Mg-0.4Dy alloys in the deformation and annealing conditions resulted from the non-equilibrium conditions during alloy casting and their fragmentation during HPT processing (see Figure 5) since the solubility of Gd and Dy in the Mg matrix is relatively high with a value of 23.4 and 25.2%, respectively [64]. Therefore, it is expected that the presence of metastable phases in solid solution alloys such as the

Mg-0.6Gd and Mg-0.4Dy alloys will have less effect on the evolution of microstructure during the deformation and annealing treatments.

The restricted DRX during HPT processing of the Mg-1.4Nd alloy led to a more homogenous grain size distribution by comparison with the bimodal microstructure of the annealed Mg-0.4Dy sample at 450 °C (Figure 2h,i). Indeed, the homogenous recrystallisation microstructure and texture weakening of the Mg-1.4Nd alloy indicated that the deformed grains were statically recrystallised through the classical nucleation and growth mechanism [86]. The bimodal grain distributions for the Mg-0.6Gd and Mg-0.4Dy samples can be explained because the DRX grains will undergo grain growth during annealing and simultaneously the remaining deformation zones will statically recrystallize through the classical nucleation and growth mechanism. In addition, the absence of DRX is the mean reason for the weakening of the recrystallisation texture. A similar connection between texture weakening and limited DRX was observed in deformed and annealed Mg-based alloys [10,87,88]. In practice, limited DRX during deformation means a high stored energy and it is now well known that the possibility to have recrystallisation nuclei with a variety of orientations increases with increasing stored energy [89,90].

It is worth noting that the mean grain size of the annealed Mg-1.4Nd sample at 450 °C (~38 μm) was relatively larger than for the annealed Mg-0.6Gd (~20 μm) and Mg-0.4Dy (~15.5 μm) samples at 450 °C indicating that the static recrystallisation kinetics is faster in Mg-1.4Nd alloy than in Mg-0.6Gd and Mg-0.4Dy alloys. Hence, it can be concluded from this observation that depicts the fact that the Nd element has a strong impact on inhibiting DRX during HPT processing, but it seems to have less effect on static recrystallisation and grain growth. Moreover, such an observation demonstrates that the absence of DRX is more related to the fraction of nucleation sites rather than to the grain growth rate. It is reasonable to expect that the grain growth rate will depend on the nature of the grain boundaries. As is shown in Figure 4, the grain boundary misorientation angle distribution of Mg-1.4Nd changed significantly after annealing at 450 °C for 1 h. The role of RE elements on the grain boundary character will be subject for a future work.

Apparently, the occurrence of precipitation during annealing at 450 °C of the Mg-1.4Nd alloy failed to restrict the grain boundary migration in the alloy. A close inspection of Figure 5g indicated that the precipitation and their coarsening occur inside the grains rather than at the grain boundaries which explains the negative effect of precipitation on the grain size of the Mg-1.4Nd alloy.

4.2. Corrosion Behaviour

The electrochemical results shown in Figures 7 and 8 and Tables 1 and 2 demonstrate that the Mg-1.4Nd, Mg-0.6Gd, and Mg-0.4Dy alloys under HPT processing and isochronal annealing exhibit a similar corrosion mechanism consisting of the formation of a protective corrosion product and localised corrosion (or pitting corrosion) but with different corrosion rates. It is apparent that the Mg-0.6Gd alloy shows better corrosion resistance, followed by Mg-0.4Dy, and then the Mg-1.4Nd alloy. It seems that the heavy RE (Gd and Dy) elements have the ability to better protect the surface of the Mg matrix compared with the light RE elements (Nd). Similar observation was noticed earlier in comparing the corrosion performance of Mg-0.4Dy and Mg-1.43La (wt.%) alloys [13]. Nevertheless, Table 2 shows that the corrosion resistance of the annealed Mg-1.4Nd at 450 °C (149.9 Ω.cm^2) is higher than for the Mg-0.4Dy alloy under the same annealing condition (70.2 Ω.cm^2). This indicates that the evolution of microstructure during thermomechanical processing affects more the corrosion performance of the alloy than the RE alloying element.

The corrosion resistance decreases for the Mg-1.4Nd alloy in the following order: HPT-processed, annealed at 450 °C, and then annealed at 250 °C. In contrast, the corrosion resistance decreases for Mg-0.6Gd and Mg-0.4Dy alloys in the following order: HPT-processed, annealed at 250 °C, and annealed at 450 °C.

The present results show that HPT processing of the three Mg–RE alloys has a better impact on the corrosion resistance than under annealing conditions, where this is primarily

due to the grain refinement and the presence of deformation features such as twins and the high density of dislocations. Indeed, it was found that the presence of twins in Mg-based alloys containing RE elements can be beneficial for improving corrosion resistance due to the high chemical activity of these RE elements [49]. In addition, the grain refinement leads to an increase in the number of grain boundaries that act as barriers for preferential crystallographic pitting corrosion and assist in the formation of a stable passivation layer on the surface of fine grains [34].

To analyze the effect of grain size on the corrosion resistance of these Mg–RE alloys, the E_{corr} was connected with the mean grain size, d, based on a Hall–Petch type relationship as follows [91,92]:

$$E_{corr} = A + \frac{B}{\sqrt{d}} \tag{5}$$

where A and B are constant depending on the environment and the material.

The evolution of potential corrosion as a function of the inverse of the square root of the mean grain size for Mg-1.4Nd, Mg-0.6Gd, and Mg-0.4Dy alloys is displayed in Figure 10. Thus, there is a linear relationship between E_{corr} and $d^{-1/2}$ for the Mg-0.6Gd and Mg-0.4Dy alloys. The decrease of corrosion resistance for these two alloys with increasing annealing temperature is due primarily to the increase in grain size due to the static recrystallisation and grain growth process. The elimination of dislocations through an annealing treatment may be another reason for the decrease in the corrosion resistance. Nevertheless, the Hall–Petch type relationship is not valid for the Mg-1.4Nd alloy indicating that the grain size is not the only microstructural parameter affecting the corrosion behaviour of this alloy. In fact, the present results show that the heat treatment at 450 °C for 1 h of the HPT-processed Mg-1.4Nd sample causes precipitation and the coarsening of second phases (Figure 5) together with a weakening of texture (Figure 6) which may be the reasons for the improved corrosion resistance compared with the sample heat treated at 250 °C for 1 h.
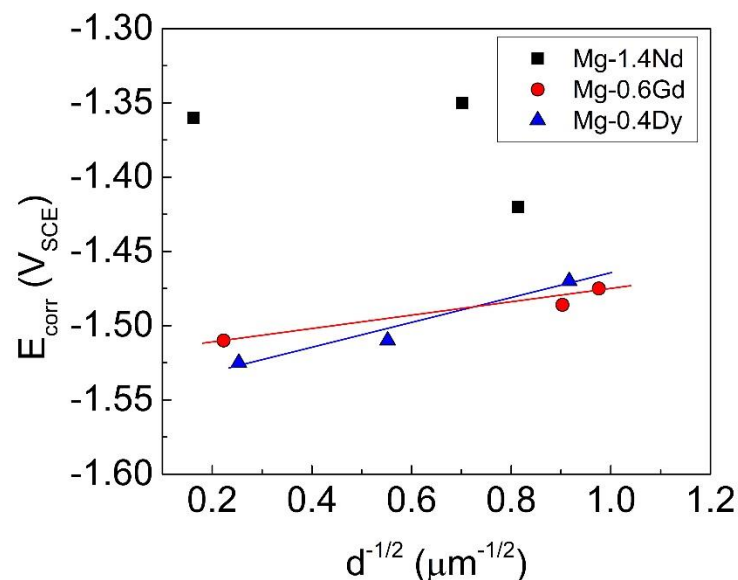
Figure 10. Evolution of E_{corr} as a function of $d^{-1/2}$ for HPT-processed and annealed Mg-1.4Nd, Mg-0.6Gd, and Mg-0.4Dy samples.

It is expected that the presence of twins in the HPT-processed Mg-1.4Nd sample acts as preferential sites for precipitation during annealing at 450 °C and this improves the corrosion resistance. More importantly, the high chemical activity of RE elements can change the role of second phases from micro-cathode as in traditional Mg–Al alloys [82,93] to micro-anodes leading to a decrease in the corrosion rate of the Mg matrix [94,95].

As noted in the introduction, the characteristics of the microstructures may or may not be advantageous for the corrosion performance of Mg-based alloys [34,49]. Based on

the present results, it is concluded that the binary Mg-1.4Nd, Mg-0.6Gd, and Mg-0.4Dy alloys belong to the alloy category where grain refinement, deformation features, and the presence of second phases are helpful in improving the corrosion resistance of Mg.

5. Summary and Conclusions

The microstructure, texture, and their impact on the corrosion behaviour of low LREE-containing Mg-1.4Nd alloy and low HREE-containing Mg-0.6Gd and Mg-0.4Dy alloys were comprehensively examined after HPT processing and isochronal annealing at 250 and 450 °C for 1 h. The important conclusions are as follows:

DRX was restricted in the HPT-processed Mg-1.4Nd alloy by comparison with the HPT-processed Mg-0.6Gd and Mg-0.4Dy alloys. Consequently, the deformation microstructure of the Mg-1.4Nd alloy was heterogenous and characterised by the presence of extension twins and the sub-grain development (SGD) mechanism. By contrast, the deformation microstructures of the Mg-0.6Gd and Mg-0.4Dy alloys were homogenous and formed of reasonably equiaxed grains.

Annealing at 450 °C for 1 h led to a homogenous equiaxed microstructure and weak basal texture for the Mg-1.4Nd alloy whereas for the Mg-0.6Gd and Mg-0.4Dy alloys there was an heterogenous bimodal microstructure and stable basal texture. Precipitation and their coarsening have no effect on grain boundary migration and the restriction of grain size.

The microstructures of the three alloys were relatively thermally stable through annealing at 250 °C for 1 h.

HREE (Gd and Dy) elements tend to have better corrosion resistance than the LREE (Nd) element. Nevertheless, precipitation coarsening in Mg-1.4Nd alloy can change this tendency.

The corrosion improvement of the low LREE-containing Mg–RE alloy is controlled by grain refinement, precipitation coarsening, and texture weakening. Only the grain refinement mechanism was noticed in the low HREE-containing Mg–RE alloy.

Institutional Review Board Statement: Not applicable.

Informed Consent Statement: Not applicable.

Data Availability Statement: The data presented in this study are available upon request from the corresponding author.

Conflicts of Interest: The authors declare no conflict of interest.

References

1. Song, J.; Chen, J.; Xiong, X.; Peng, X.; Chen, D.; Pan, F. Research advances of magnesium and magnesium alloys worldwide in 2021. *J. Magnes. Alloy.* **2022**, *10*, 863–898. [CrossRef]
2. Shi, B.; Yang, C.; Peng, Y.; Zhang, F.; Pan, F. Anisotropy of wrought magnesium alloys: A focused overview. *J. Magnes. Alloy.* **2022**, *10*, 1476–1510. [CrossRef]
3. Agnew, S.R.; Yoo, M.H.; Tomé, C.N. Application of texture simulation to understanding mechanical behavior of Mg and solid solution alloys containing Li or Y. *Acta Mater.* **2001**, *49*, 4277–4289. [CrossRef]
4. Chino, Y.; Kado, M.; Mabuchi, M. Enhancement of tensile ductility and stretch formability of magnesium by addition of 0.2 wt% (0.035at%) Ce. *Mater. Sci. Eng. A* **2008**, *494*, 343–349. [CrossRef]

5. Sandlöbes, S.; Friák, M.; Neugebauer, J.; Raabe, D. Basal and non-basal dislocation slip in Mg–Y. *Mater. Sci. Eng. A* **2013**, *576*, 61–68. [CrossRef]

6. Stanford, N.; Atwell, D.; Barnett, M.R. The effect of Gd on the recrystallisation, texture and deformation behaviour of magnesium-based alloys. *Acta Mater.* **2010**, *58*, 6773–6783. [CrossRef]

7. Hadorn, J.P.; Hantzsche, K.; Yi, S.; Bohlen, J.; Letzig, D.; Wollmershauser, J.A.; Agnew, S.R. Role of Solute in the Texture Modification During Hot Deformation of Mg-Rare Earth Alloys. *Metall. Mater. Trans. A* **2012**, *43*, 1347–1362. [CrossRef]

8. Guerza-Soualah, F.; Azzeddine, H.; Baudin, T.; Helbert, A.-L.; Brisset, F.; Bradai, D. Microstructural and textural investigation of an Mg–Dy alloy after hot plane strain compression. *J. Magnes. Alloy.* **2020**, *8*, 1198–1207. [CrossRef]

9. Guerza-Soualah, F.; Hanna, A.; Azzeddine, H.; Helbert, A.-L.; Brisset, F.; Baudin, T.; Bradai, D. The deformation and recrystallization behaviour of an Mg-Dy alloy processed by plane strain compression. *Mater. Today Commun.* **2020**, *24*, 101239. [CrossRef]

10. Molodov, K.D.; Al-Samman, T.; Molodov, D.A. Effect of gadolinium on the deformation and recrystallization behavior of magnesium crystals. *Acta Mater.* **2022**, *240*, 118312. [CrossRef]

11. Arrabal, R.; Matykina, E.; Pardo, A.; Merino, M.C.; Paucar, K.; Mohedano, M.; Casajús, P. Corrosion behaviour of AZ91D and AM50 magnesium alloys with Nd and Gd additions in humid environments. *Corros. Sci.* **2012**, *55*, 351–362. [CrossRef]

12. Meng, J.; Sun, W.; Tian, Z.; Qiu, X.; Zhang, D. 2—Corrosion performance of magnesium (Mg) alloys containing rare-earth (RE) elements. In *Corrosion Prevention of Magnesium Alloys*; Song, G.-L., Ed.; Woodhead Publishing: Sawston, UK, 2013; pp. 38–60.

13. Azzeddine, H.; Hanna, A.; Dakhouche, A.; Rabahi, L.; Scharnagl, N.; Dopita, M.; Brisset, F.; Helbert, A.-L.; Baudin, T. Impact of rare-earth elements on the corrosion performance of binary magnesium alloys. *J. Alloys Compd.* **2020**, *829*, 154569. [CrossRef]

14. Chi, Y.C.; Guan, B.R.; Chen, F.; Qin, F.X. Effect of RE Elements Addition on Corrosion Behavior of Mg-Zn-Ca Amorphous Alloys for Biomedical Applications. *Mater. Sci. Forum* **2021**, *1035*, 501–510. [CrossRef]

15. Xie, J.; Zhang, J.; You, Z.; Liu, S.; Guan, K.; Wu, R.; Wang, J.; Feng, J. Towards developing Mg alloys with simultaneously improved strength and corrosion resistance via RE alloying. *J. Magnes. Alloy.* **2021**, *9*, 41–56. [CrossRef]

16. Tan, J.; Ramakrishna, S. Applications of Magnesium and Its Alloys: A Review. *Appl. Sci.* **2021**, *11*, 6861. [CrossRef]

17. Powell, B.R.; Krajewski, P.E.; Luo, A.A. Chapter 4—Magnesium alloys for lightweight powertrains and automotive structures. In *Materials, Design and Manufacturing for Lightweight Vehicles*, 2nd ed.; Mallick, P.K., Ed.; Woodhead Publishing: Sawston, UK, 2021; pp. 125–186.

18. Staiger, M.P.; Pietak, A.M.; Huadmai, J.; Dias, G. Magnesium and its alloys as orthopedic biomaterials: A review. *Biomaterials* **2006**, *27*, 1728–1734. [CrossRef]

19. Azzeddine, H.; Hanna, A.; Dakhouche, A.; Luthringer-Feyerabend, B. Corrosion behaviour and cytocompatibility of selected binary magnesium-rare earth alloys. *J. Magnes. Alloy.* **2021**, *9*, 581–591. [CrossRef]

20. Stanford, N. Micro-alloying Mg with Y, Ce, Gd and La for texture modification—A comparative study. *Mater. Sci. Eng. A* **2010**, *527*, 2669–2677. [CrossRef]

21. Long, L.J.; Huang, G.H.; Yin, D.D.; Ji, B.; Zhou, H.; Wang, Q.D. Effects of Y on the Deformation Mechanisms of Extruded Mg-Y Sheets During Room-Temperature Compression. *Metall. Mater. Trans. A* **2020**, *51*, 2738–2751. [CrossRef]

22. Xu, Y.; Gavras, S.; Gensch, F.; Kainer, K.U.; Hort, N. Effect of Nd Additions on the Mechanical Properties of Mg Binary Alloys. *JOM* **2020**, *72*, 517–525. [CrossRef]

23. Sheikhani, A.; Roumina, R.; Mahmudi, R. Texture softening in a rare earth elements-containing AZ31 magnesium alloy during hot compression deformation. *J. Mater. Res. Technol.* **2022**, *18*, 4089–4098. [CrossRef]

24. Mirzakhani, A.; Assempour, A. The effects of microstructural parameters on the tension-compression mechanical behavior of extruded Mg-XY rods using crystal plasticity finite element modeling. *Results Eng.* **2023**, *17*, 100834. [CrossRef]

25. Zhou, S.; Tang, A.; Liu, T.; Peng, P.; Zhang, J.; She, J.; Pan, F. Ductility enhancement by activating non-basal slip in as-extruded Mg alloys with dilute Sc addition. *J. Mater. Res. Technol.* **2023**, *22*, 3362–3374. [CrossRef]

26. Zhilyaev, A.P.; Langdon, T.G. Using high-pressure torsion for metal processing: Fundamentals and applications. *Prog. Mater. Sci.* **2008**, *53*, 893–979. [CrossRef]

27. Huang, Y.; Figueiredo, R.B.; Baudin, T.; Brisset, F.; Langdon, T.G. Evolution of Strength and Homogeneity in a Magnesium AZ31 Alloy Processed by High-Pressure Torsion at Different Temperatures. *Adv. Eng. Mater.* **2012**, *14*, 1018–1026. [CrossRef]

28. Valiev, R.Z.; Estrin, Y.; Horita, Z.; Langdon, T.G.; Zechetbauer, M.J.; Zhu, Y.T. Producing bulk ultrafine-grained materials by severe plastic deformation. *JOM* **2006**, *58*, 33–39. [CrossRef]

29. Figueiredo, R.B.; Langdon, T.G. Fabricating Ultrafine-Grained Materials through the Application of Severe Plastic Deformation: A Review of Developments in Brazil. *J. Mater. Res. Technol.* **2012**, *1*, 55–62. [CrossRef]

30. Huang, Y.; Langdon, T.G. Advances in ultrafine-grained materials. *Mater. Today* **2013**, *16*, 85–93. [CrossRef]

31. Wongsa-Ngam, J.; Kawasaki, M.; Langdon, T.G. A comparison of microstructures and mechanical properties in a Cu–Zr alloy processed using different SPD techniques. *J. Mater. Sci.* **2013**, *48*, 4653–4660. [CrossRef]

32. Figueiredo, R.B.; Langdon, T.G. Deformation mechanisms in ultrafine-grained metals with an emphasis on the Hall–Petch relationship and strain rate sensitivity. *J. Mater. Res. Technol.* **2021**, *14*, 137–159. [CrossRef]

33. Azzeddine, H.; Bradai, D.; Baudin, T.; Langdon, T.G. Texture evolution in high-pressure torsion processing. *Prog. Mater. Sci.* **2022**, *125*, 100886. [CrossRef]

34. Bahmani, A.; Lotfpour, M.; Taghizadeh, M.; Kim, W.-J. Corrosion behavior of severely plastically deformed Mg and Mg alloys. *J. Magnes. Alloy.* **2022**, *10*, 2607–2648. [CrossRef]

35. Nazeer, F.; Long, J.; Yang, Z.; Li, C. Superplastic deformation behavior of Mg alloys: A-review. *J. Magnes. Alloy.* **2022**, *10*, 97–109. [CrossRef]

36. Kai, M.; Horita, Z.; Langdon, T.G. Developing grain refinement and superplasticity in a magnesium alloy processed by high-pressure torsion. *Mater. Sci. Eng. A* **2008**, *488*, 117–124. [CrossRef]

37. Huang, Y.; Figueiredo, R.B.; Baudin, T.; Helbert, A.-L.; Brisset, F.; Langdon, T.G. Effect of temperature on the processing of a magnesium alloy by high-pressure torsion. *J. Mater. Sci.* **2012**, *47*, 7796–7806. [CrossRef]

38. Meng, F.; Rosalie, J.M.; Singh, A.; Somekawa, H.; Tsuchiya, K. Ultrafine grain formation in Mg–Zn alloy by in situ precipitation during high-pressure torsion. *Scr. Mater.* **2014**, *78–79*, 57–60. [CrossRef]

39. Alsubaie, S.A.; Bazarnik, P.; Lewandowska, M.; Huang, Y.; Langdon, T.G. Evolution of microstructure and hardness in an AZ80 magnesium alloy processed by high-pressure torsion. *J. Mater. Res. Technol.* **2016**, *5*, 152–158. [CrossRef]

40. Alizadeh, R.; Mahmudi, R.; Ngan, A.H.W.; Huang, Y.; Langdon, T.G. Superplasticity of a nano-grained Mg–Gd–Y–Zr alloy processed by high-pressure torsion. *Mater. Sci. Eng. A* **2016**, *651*, 786–794. [CrossRef]

41. Sun, W.T.; Qiao, X.G.; Zheng, M.Y.; Zhao, X.J.; Chen, H.W.; Gao, N.; Starink, M.J. Achieving ultra-high hardness of nanostructured Mg-8.2Gd-3.2Y-1.0Zn-0.4Zr alloy produced by a combination of high pressure torsion and ageing treatment. *Scr. Mater.* **2018**, *155*, 21–25. [CrossRef]

42. Sun, W.T.; Qiao, X.G.; Zheng, M.Y.; He, Y.; Hu, N.; Xu, C.; Gao, N.; Starink, M.J. Exceptional grain refinement in a Mg alloy during high pressure torsion due to rare earth containing nanosized precipitates. *Mater. Sci. Eng. A* **2018**, *728*, 115–123. [CrossRef]

43. Hanna, A.; Azzeddine, H.; Lachhab, R.; Baudin, T.; Helbert, A.-L.; Brisset, F.; Huang, Y.; Bradai, D.; Langdon, T.G. Evaluating the textural and mechanical properties of an Mg-Dy alloy processed by high-pressure torsion. *J. Alloys Compd.* **2019**, *778*, 61–71. [CrossRef]

44. Li, Y.; Qu, C.; Wang, J.; Xu, R. Exceptional aging hardening behaviour of nanocrystalline Mg–Y-Nd-Gd-Zr alloy prepared by high pressure torsion. *J. Alloys Compd.* **2020**, *813*, 152123. [CrossRef]

45. Zhang, N.X.; Kawasaki, M.; Ding, H.; Langdon, T.G. An examination of microstructural evolution and homogeneity in a magnesium AZ80 alloy processed by high-pressure torsion. *Mater. Sci. Eng. A* **2021**, *806*, 140832. [CrossRef]

46. Silva, C.L.P.; Soares, R.B.; Pereira, P.H.R.; Figueiredo, R.B.; Lins, V.F.C.; Langdon, T.G. The Effect of High-Pressure Torsion on Microstructure, Hardness and Corrosion Behavior for Pure Magnesium and Different Magnesium Alloys. *Adv. Eng. Mater.* **2019**, *21*, 1801081. [CrossRef]

47. Kasaeian-Naeini, M.; Sedighi, M.; Hashemi, R. Severe plastic deformation (SPD) of biodegradable magnesium alloys and composites: A review of developments and prospects. *J. Magnes. Alloy.* **2022**, *10*, 938–955. [CrossRef]

48. Gerashi, E.; Alizadeh, R.; Langdon, T.G. Effect of crystallographic texture and twinning on the corrosion behavior of Mg alloys: A review. *J. Magnes. Alloy.* **2022**, *10*, 313–325. [CrossRef]

49. Li, L.; Liu, W.; Qi, F.; Wu, D.; Zhang, Z. Effects of deformation twins on microstructure evolution, mechanical properties and corrosion behaviors in magnesium alloys—A review. *J. Magnes. Alloy.* **2022**, *10*, 2334–2353. [CrossRef]

50. Mohammadi Zerankeshi, M.; Alizadeh, R.; Gerashi, E.; Asadollahi, M.; Langdon, T.G. Effects of heat treatment on the corrosion behavior and mechanical properties of biodegradable Mg alloys. *J. Magnes. Alloy.* **2022**, *10*, 1737–1785. [CrossRef]

51. Yang, L.; Huang, Y.; Feyerabend, F.; Willumeit, R.; Mendis, C.; Kainer, K.U.; Hort, N. Microstructure, mechanical and corrosion properties of Mg–Dy–Gd–Zr alloys for medical applications. *Acta Biomater.* **2013**, *9*, 8499–8508. [CrossRef]

52. Chen, L.-Y.; Xu, J.-Q.; Choi, H.; Pozuelo, M.; Ma, X.; Bhowmick, S.; Yang, J.-M.; Mathaudhu, S.; Li, X.-C. Processing and properties of magnesium containing a dense uniform dispersion of nanoparticles. *Nature* **2015**, *528*, 539–543. [CrossRef]

53. Hanna, A.; Dakhouche, A.; Tirsatine, K.; Sari, A.; Khereddine, Y.; Bradai, D.; Azzeddine, H. Effect of hot rolling on the corrosion behavior of AZ31 magnesium alloy. *J Metall. Res. Technol.* **2019**, *116*, 109. [CrossRef]

54. Zou, G.; Peng, Q.; Wang, Y.; Liu, B. The effect of extension twinning on the electrochemical corrosion properties of Mg–Y alloys. *J. Alloys Compd.* **2015**, *618*, 44–48. [CrossRef]

55. Liu, J.; Han, E.H.; Song, Y.; Shan, D. Effect of twins on the corrosion behavior of Mg–5Y–7Gd–1Nd–0.5Zr Mg alloy. *J. Alloys Compd.* **2018**, *757*, 356–363. [CrossRef]

56. Sakai, T.; Belyakov, A.; Kaibyshev, R.; Miura, H.; Jonas, J.J. Dynamic and post-dynamic recrystallization under hot, cold and severe plastic deformation conditions. *Prog. Mater. Sci.* **2014**, *60*, 130–207. [CrossRef]

57. Khodabakhshi, F.; Mohammadi, M.; Gerlich, A.P. Stability of ultra-fine and nano-grains after severe plastic deformation: A critical review. *J. Mater. Sci.* **2021**, *56*, 15513–15537. [CrossRef]

58. Hanna, A.; Azzeddine, H.; Huang, Y.; Bradai, D.; Cabrera, J.M.; Langdon, T.G. An investigation of the thermal stability of an MgDy alloy after processing by high-pressure torsion. *Mater. Charact.* **2019**, *151*, 519–529. [CrossRef]

59. Tighiouaret, S.; Lachhab, R.; Hanna, A.; Azzeddine, H.; Huang, Y.; Baudin, T.; Helbert, A.-L.; Brisset, F.; Bradai, D.; Langdon, T.G. Thermal Stability of an Mg–Nd Alloy Processed by High-Pressure Torsion. *Adv. Eng. Mater.* **2019**, *21*, 1900801. [CrossRef]

60. Liu, X.; Xu, R. Microstructure Evolution and Thermal Stability of Mg-Sm-Ca Alloy Processed by High-Pressure Torsion. *J. Mater. Eng. Perform.* **2022**, *31*, 2644–2652. [CrossRef]

61. Sun, W.; He, Y.; Qiao, X.; Zhao, X.; Chen, H.; Gao, N.; Starink, M.J.; Zheng, M. Exceptional thermal stability and enhanced hardness in a nanostructured Mg-Gd-Y-Zn-Zr alloy processed by high pressure torsion. *J. Magnes. Alloy.* **2022**. [CrossRef]

62. Wang, J.; Li, Y.; Xu, R. The thermal stability and activation energy of the nanocrystalline Mg-Zn-Y alloy obtained by high pressure torsion. *Mater. Lett.* **2020**, *268*, 127607. [CrossRef]
63. Zhang, C.; Guan, S.; Wang, L.; Zhu, S.; Chang, L. The microstructure and corrosion resistance of biological Mg–Zn–Ca alloy processed by high-pressure torsion and subsequently annealing. *J. Mater. Res.* **2017**, *32*, 1061–1072. [CrossRef]
64. Rokhlin, L.L. *Magnesium Alloys Containing Rare Earth Metals: Structure and Properties*, 1st ed.; CRC Press: London, UK, 2003; p. 256.
65. Hanna, A.; Rabahi, L.; Soualili, M.A.; Dakhouche, A.; Bradai, D.; Azzeddine, H. On the corrosion behaviour of as-cast and heat-treated Mg-RE alloys in 0.9% NaCl solution. *J. Met. Mater. Miner.* **2020**, *30*, 29–39. [CrossRef]
66. Figueiredo, R.B.; Cetlin, P.R.; Langdon, T.G. Using finite element modeling to examine the flow processes in quasi-constrained high-pressure torsion. *Mater. Sci. Eng. A* **2011**, *528*, 8198–8204. [CrossRef]
67. Cho, J.-H.; Rollett, A.D.; Oh, K.H. Determination of a mean orientation in electron backscatter diffraction measurements. *Metall. Mater. Trans. A* **2005**, *36*, 3427–3438. [CrossRef]
68. Hielscher, R.; Schaeben, H. A novel pole figure inversion method: Specification of the MTEX algorithm. *J. Appl. Cryst.* **2008**, *41*, 1024–1037. [CrossRef]
69. Klar, R.; Lücke, K. Orientierungszusammenhänge bei der Rekristallisation von Einkristallen aus Zink und Kadmium. *Int. J. Mater. Res.* **1968**, *59*, 194–202. [CrossRef]
70. Gottstein, G.; Al Samman, T. Texture Development in Pure Mg and Mg Alloy AZ31. *Mater. Sci. Forum* **2005**, *495–497*, 623–632. [CrossRef]
71. Hirsch, J.; Al-Samman, T. Superior light metals by texture engineering: Optimized aluminum and magnesium alloys for automotive applications. *Acta Mater.* **2013**, *61*, 818–843. [CrossRef]
72. Ould Mohamed, O.; Azzeddine, H.; Huang, Y.; Baudin, T.; Bazarnik, P.; Brisset, F.; Kawasaki, M.; Langdon, T.G. Investigation of Microstructure and Texture Evolution in an AZ31/Mg–Gd Alloy Hybrid Metal Fabricated by High-Pressure Torsion. *Adv. Eng. Mater.* **2023**, 2201794. [CrossRef]
73. Natarajan, A.R.; Solomon, E.L.S.; Puchala, B.; Marquis, E.A.; Van der Ven, A. On the early stages of precipitation in dilute Mg–Nd alloys. *Acta Mater.* **2016**, *108*, 367–379. [CrossRef]
74. Song, G.L.; Atrens, A. Corrosion Mechanisms of Magnesium Alloys. *Adv. Eng. Mater.* **1999**, *1*, 11–33. [CrossRef]
75. Thomaz, T.R.; Weber, C.R.; Pelegrini, T.; Dick, L.F.P.; Knörnschild, G. The negative difference effect of magnesium and of the AZ91 alloy in chloride and stannate-containing solutions. *Corros. Sci.* **2010**, *52*, 2235–2243. [CrossRef]
76. Bender, S.; Goellner, J.; Heyn, A.; Schmigalla, S. A new theory for the negative difference effect in magnesium corrosion. *Mater. Corros.* **2012**, *63*, 707–712. [CrossRef]
77. Baril, G.; Pébère, N. The corrosion of pure magnesium in aerated and deaerated sodium sulphate solutions. *Corros. Sci.* **2001**, *43*, 471–484. [CrossRef]
78. Song, Y.; Shan, D.; Chen, R.; Zhang, F.; Han, E.-H. Biodegradable behaviors of AZ31 magnesium alloy in simulated body fluid. *Mater. Sci. Eng. C* **2009**, *29*, 1039–1045. [CrossRef]
79. Li, J.; Jiang, Q.; Sun, H.; Li, Y. Effect of heat treatment on corrosion behavior of AZ63 magnesium alloy in 3.5wt.% sodium chloride solution. *Corros. Sci.* **2016**, *111*, 288–301. [CrossRef]
80. Mohajernia, S.; Hejazi, S.; Eslami, A.; Saremi, M. Modified nanostructured hydroxyapatite coating to control the degradation of magnesium alloy AZ31 in simulated body fluid. *Surf. Coat. Technol.* **2015**, *263*, 54–60. [CrossRef]
81. Liu, F.; Song, Y.-W.; Shan, D.-Y.; Han, E.-H. Corrosion behavior of AZ31 magnesium alloy in simulated acid rain solution. *Trans. Nonferrous Met. Soc. China* **2010**, *20*, s638–s642. [CrossRef]
82. Zhang, T.; Shao, Y.; Meng, G.; Cui, Z.; Wang, F. Corrosion of hot extrusion AZ91 magnesium alloy: I-relation between the microstructure and corrosion behavior. *Corros. Sci.* **2011**, *53*, 1960–1968. [CrossRef]
83. Sitdikov, O.; Kaibyshev, R.; Sakai, T. Dynamic Recrystallization Based on Twinning in Coarse-Grained Mg. *Mater. Sci. Forum* **2003**, *419–422*, 521–526. [CrossRef]
84. Galiyev, A.; Kaibyshev, R.; Gottstein, G. Correlation of plastic deformation and dynamic recrystallization in magnesium alloy ZK60. *Acta Mater.* **2001**, *49*, 1199–1207. [CrossRef]
85. Zhang, Q.; Fan, T.-W.; Fu, L.; Tang, B.-Y.; Peng, L.-M.; Ding, W.-J. Ab-initio study of the effect of rare-earth elements on the stacking faults of Mg solid solutions. *Intermetallics* **2012**, *29*, 21–26. [CrossRef]
86. Humphreys, J.; Rohrer, G.S.; Rollett, A. Chapter 7—Recrystallization of Single-Phase Alloys. In *Recrystallization and Related Annealing Phenomena*, 3rd ed.; Humphreys, J., Rohrer, G.S., Rollett, A., Eds.; Elsevier: Oxford, UK, 2017; pp. 245–304.
87. Tighiouaret, S.; Hanna, A.; Azzeddine, H.; Rabahi, L.; Dakhouche, A.; Brisset, F.; Helbert, A.-L.; Baudin, T.; Bradai, D. On the evolution of microstructure, texture and corrosion behavior of a hot-rolled and annealed AZ31 alloy. *Mater. Chem. Phys.* **2021**, *267*, 124598. [CrossRef]
88. Su, J.; Yue, S. Texture Weakening and Grain Refinement by High Speed Rolling and Annealing of an AZ31 Magnesium Alloy. In *Proceedings of the Magnesium Technology 2017*; Springer International Publishing: Berlin/Heidelberg, Germany, 2017; pp. 547–554.
89. Jung, I.-H.; Sanjari, M.; Kim, J.; Yue, S. Role of RE in the deformation and recrystallization of Mg alloy and a new alloy design concept for Mg–RE alloys. *Scr. Mater.* **2015**, *102*, 1–6. [CrossRef]
90. Sadi, S.; Hanna, A.; Baudin, T.; Brisset, F.; Cabrera, J.M.; Azzeddine, H. Microstructure and texture evolution of ECAP-processed Mg-Ce alloy during isothermal annealing. *Mater. Today Commun.* **2022**, *32*, 103920. [CrossRef]

91. Ralston, K.D.; Fabijanic, D.; Birbilis, N. Effect of grain size on corrosion of high purity aluminium. *Electrochim. Acta* **2011**, *56*, 1729–1736. [CrossRef]

92. Ralston, K.D.; Birbilis, N.; Davies, C.H.J. Revealing the relationship between grain size and corrosion rate of metals. *Scr. Mater.* **2010**, *63*, 1201–1204. [CrossRef]

93. Zhang, T.; Meng, G.; Shao, Y.; Cui, Z.; Wang, F. Corrosion of hot extrusion AZ91 magnesium alloy. Part II: Effect of rare earth element neodymium (Nd) on the corrosion behavior of extruded alloy. *Corros. Sci.* **2011**, *53*, 2934–2942. [CrossRef]

94. Liu, J.; Song, Y.; Chen, J.; Chen, P.; Shan, D.; Han, E.-H. The Special Role of Anodic Second Phases in the Micro-galvanic Corrosion of EW75 Mg Alloy. *Electrochim. Acta* **2016**, *189*, 190–195. [CrossRef]

95. Cai, C.; Song, R.; Wang, L.; Li, J. Effect of anodic T phase on surface micro-galvanic corrosion of biodegradable Mg-Zn-Zr-Nd alloys. *Appl. Surf. Sci.* **2018**, *462*, 243–254. [CrossRef]